

The Different Dynamic Influences of Typhoon Kalmaegi on two Pre-existing Anticyclonic Ocean Eddies

Yihao He¹, Xiayan Lin^{1,2,*}, Guoqing Han¹, Yu Liu^{1,3} and Han Zhang^{2,3,*}

¹ Marine Science and Technology College, Zhejiang Ocean University, Zhoushan 316022, China;

² State Key Laboratory of Satellite Ocean Environment Dynamics, Second Institute of Oceanography, Ministry of Natural Resources, Hangzhou 310012, China;

³ Southern Marine Science and Engineering Guangdong Laboratory (Zhuhai), Zhuhai 519082, China

**Correspondence:* Xiayan Lin (linxiayan@zjou.edu.cn) and Han Zhang (zhanghan@sio.org.cn)

Abstract: Using multi-source observational data and GLORYS12V1 reanalysis data, we conduct a comparative analysis of different responses of two warm eddies, AE1 and AE2 in the northern South China Sea to Typhoon Kalmaegi during September 2014. The findings of our research are as follows: (1) For horizontal distribution, the area and the sea surface temperature (SST) of AE1 and AE2 decrease by about 31% (36%) and 0.4 °C (0.6 °C). The amplitude, Rossby number (R_o =relative vorticity/Coriolis parameter) and eddy kinetic energy (EKE) of AE1 increases by 1.3 cm (5.7%), 1.4×10^{-2} (20.6%) and $107.2 \text{ cm}^2 \text{ s}^{-2}$ (49.2%) after the typhoon, respectively, while AE2 weakens and the amplitude, Rossby number and EKE decreased by 3.1 cm (14.6%), 1.6×10^{-2} (26.2%) and $38.5 \text{ cm}^2 \text{ s}^{-2}$ (20.2%), respectively. (2) In vertical direction, AE1 demonstrates enhanced convergence, leading to an increase in temperature and a decrease in salinity above 150 m. The response below the mixing layer depth (MLD) is particularly prominent (1.3 °C). In contrast, AE2 experiences cooling and a decrease in salinity above the MLD. Below the MLD, it exhibits a subsurface temperature drop and salinity increase due to the upwelling of cold water induced by the suction effect of the typhoon. (3) The disparity in the responses of the two warm eddies can be attributed to their different positions relative to Typhoon Kalmaegi. Warm eddy AE1, with its center to the left of the typhoon's path, experiences a positive work effect as the typhoon passed by. The negative wind stress curl in AE1 triggers a negative Ekman pumping velocity (EPV), further enhancing the converging sinking of the upper warm water, thereby strengthening AE1. On the other hand, warm eddy AE2, situated closer to the center of the typhoon, weakens due to the cold suction caused by the strong positive wind stress curl in the typhoon's center. Same polarity eddies may have different responses to typhoons. The distance between eddies and typhoons, eddies intensity and the background field need to be considered.

31 **1. Introduction**

32 Tropical cyclones (TCs), as they traverse the vast ocean, interact with oceanic mesoscale processes,
33 particularly with mesoscale eddies, representing a crucial aspect of air-sea interaction (Shay and Jaimes,
34 2010; Lu et al., 2016; Song et al., 2018; Ning et al., 2019; Sun et al., 2023). The South China Sea (SCS)
35 experiences an average of six TCs passing through each year (Wang et al., 2007), causing prominent
36 exchange of energy and mass between air and sea (Price, 1981). Meanwhile, due to the influence of the
37 Asian monsoon, intrusion of the Kuroshio Current, and complex topography, the Northern South China
38 Sea (NSCS) also encounters frequent eddy activities (Xiu et al., 2010; Chen et al., 2011). These
39 mesoscale oceanic eddies often play significant roles in mass and heat transport and air-sea interaction.
40 This unique setting offers an exceptional opportunity to investigate the generation, evolution, and
41 termination of mesoscale eddies and their interaction with TCs.

42 Pre-existing mesoscale eddies play a crucial role in the feedback mechanism between the ocean and
43 TCs. Cyclonic eddies (cold eddies) enhance the sea surface cooling effect under TCs conditions, resulting
44 in TCs weakening, due to their thermodynamic structures and cold-water entrainment processes that
45 reduce the heat transfer from the sea surface to the TCs through air-sea interaction (Ma et al., 2017; Yu
46 et al., 2021). In contrast, anticyclonic eddies (warm eddies) suppress this cooling effect, leading to TCs
47 intensification (Shay et al., 2000; Walker et al., 2005; Lin et al., 2011; Wang et al., 2018). Warm eddies
48 have a thicker upper mixed layer, which stores more heat. When a TC passes over a warm eddy, it
49 increases sensible heat and water vapor in TC's center, which are closely related to the TC's
50 intensification (Wada and Usui, 2010; Huang et al., 2022). Furthermore, the downwelling within warm
51 eddies hinders the upwelling of cold water, reducing the apparent sea surface cooling caused by the TCs.
52 These processes weaken the oceanic negative feedback effect and help to sustain or even strengthen TC's
53 development. TCs cause the strengthening of cyclonic eddies, leading to positive potential vorticity
54 anomalies (Zhang et al, 2020).

55 On the other hand, TCs also have a notable impact on the intensity, size, and movement of mesoscale
56 eddies. In general, TCs strengthen cold eddies and can even lead to the formation of new cyclonic eddies
57 in certain situations (Sun et al., 2014), while TCs accelerate the dissipation of anticyclonic eddies (Zhang
58 et al., 2020). The strengthening effect of TCs on cold eddies is related to the positions between cold
59 eddies and TCs, the intensity of eddies, and TC-induced geostrophic response (Lu et al., 2016; Yu et al.,

60 2019; Lu et al., 2023). Cyclonic eddies on the left side of the TC's track were more intensely affected by
61 the TC, and eddies with shorter lifespans or smaller radii are more susceptible to the influence of TCs.
62 The dynamic adjustment process of eddy and the upwelling induced by TC itself leads to changes in the
63 three-dimensional structure of the cyclonic eddies, including ellipse deformation and re-
64 axisymmetrization on the horizontal plane, resulting in eddy intensification. The presence of cold eddies
65 not only exacerbates the sea surface cooling in the post-TC cold eddy region but also accompanies a
66 decrease in sea level anomaly (SLA), deepening of the mixed layer, a strong cooling in the subsurface,
67 increased chlorophyll-a concentration within the eddy, and substantial increases in EKE and available
68 potential energy (Shang et al., 2015; Liu and Tang, 2018; Li et al., 2021; Ma et al., 2021).

69 Generally, TCs lead to a reduction of warm eddies, while the sea surface cooling is not significant,
70 typically within 1°C. However, there is a noticeable cooling and increased salinity in the subsurface layer,
71 accompanied by an upward shift of the 20°C isotherm, a decrease in heat and kinetic energy (Lin et al.,
72 2005; Liu et al., 2017; Huang and Wang, 2022). Lu et al. (2020) propose that TCs primarily generate
73 potential vorticity input through the geostrophic response. When a TC passes over an eddy, there is a
74 significant positive wind stress curl within the TC's maximum wind radius, which induces upwelling in
75 the mixed layer due to the divergence of the wind-driven flow field. This upward flow compresses the
76 thickness of the isopycnal layers below the mixed layer, resulting in a positive potential vorticity anomaly.
77 By analyzing the time series of ocean kinetic energy, available potential energy (APE), vorticity budget,
78 and potential vorticity (PV) budget, Rudzin and Chen (2022) find that the positive vertical vorticity
79 advection caused the TC to eliminate the warm eddy from bottom to top after passing through. Under
80 the interaction of the strong TC wind stress in the eye area of the TC and the subsurface ocean current
81 field, the early-onset of a near-inertial wake caused the disappearance of the warm eddy. However, the
82 projection of TC wind stress onto the eddy and the relative position of the warm eddy to the TC can lead
83 to different responses. According to the classical description of TC-induced upwelling, strong upwelling
84 occurs within twice the maximum wind radius of the TC center, while weak subsidence exists in the vast
85 area outside the upwelling region (Price, 1981; Jullien et al., 2012). The warm eddy located directly
86 beneath the TC's path weakens due to the cold suction caused by the TC's center. However, for warm
87 eddies located beyond twice the maximum wind radius, they are influenced by the TC's wind stress curl
88 and the downwelling within the eddy itself, resulting in the convergence of warm water in the upper

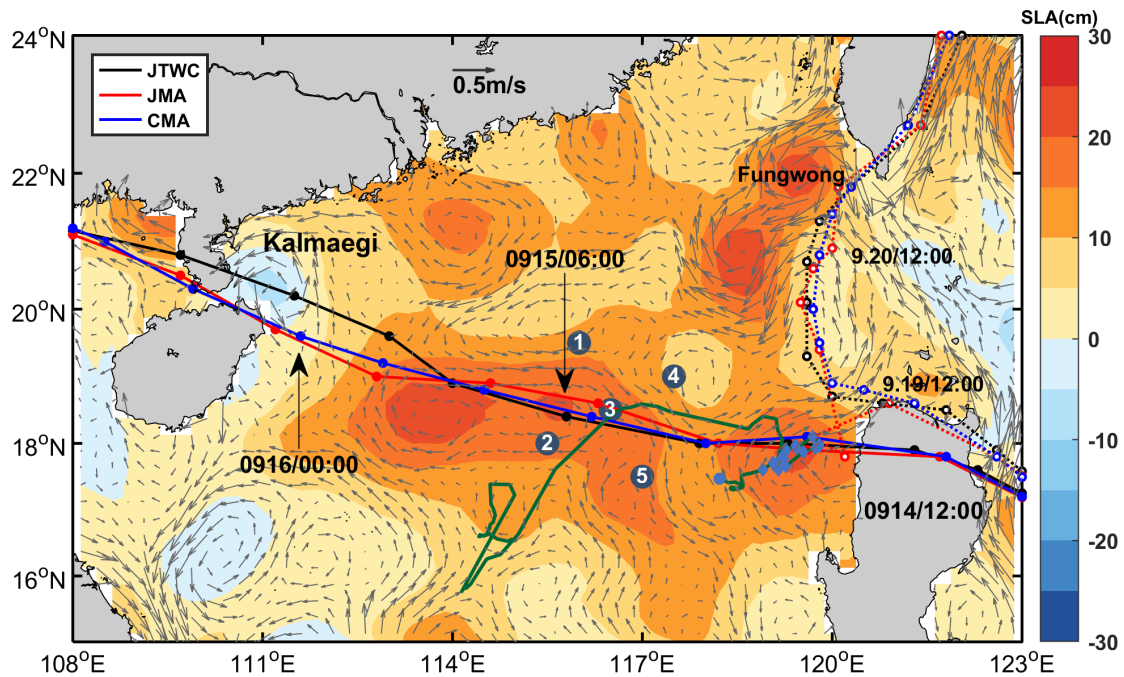
89 layers of the eddy, an increase in mixed layer thickness, and an increase in heat content, leading to a
90 warming response to the TC (Jaimes and Shay, 2015).

91 The NSCS encounters high frequency and intense TCs, concurrently, there is notable activity of
92 mesoscale eddies in this region. Based on in-situ datasets, multi-platform satellite measurements, and
93 GLORYS12V1 reanalysis data, we investigate how the upper ocean in two anticyclonic eddies responds
94 to Typhoon Kalmaegi. This marks the initial effort to characterize the different physical variations
95 induced by TCs within two same polarity eddies, contributing to a better understanding of the role played
96 by mesoscale eddies in modulating interactions between TCs and the ocean. Section 2 provides an
97 overview of the data and methods utilized in this research. Section 3 analyzes the physical parameters of
98 warm eddies, vertical temperature and salinity variations, and explores the different responses of warm
99 eddies both inside and outside the typhoon affected region. Section 4 offers a comprehensive discussion
100 and Section 5 gives a summary.

101 **2. Data and Methods**

102 **2.1. Data**

103 The six-hourly best-track typhoon datasets are obtained from the Joint Typhoon Warning Center
104 (JTWC, <http://www.usno.navy.mil/JTWC>, last access: 3 February, 2021), the Japan Meteorological
105 Agency (JMA, <https://www.jma.go.jp/jma/jma-eng/jma-center/rsmc-hp-pub-eg/besttrack.html>, last
106 access: 3 February, 2021), and the China Meteorological Administration (CMA,
107 <http://tcdata.typhoon.gov.cn>, last access: 3 February, 2022). The data contain the TCs' center locations,
108 the minimum central pressure, maximum sustained wind speed, and intensity category. The translation
109 speed of typhoons is calculated by dividing the distance travelled by each typhoon within a 6-hour
110 interval by the corresponding time. In this paper, Typhoon Kalmaegi and tropical storm Fung-wong are
111 studied (Fig. 1).



113 **Figure 1.** The tracks of Typhoon Kalmaegi (solid lines with dots) and tropical storm Fung-wong (dashed lines with
 114 hollow dots) as provide by the Joint Typhoon Warning Center (JTWC, black), Japan Meteorological Agency (JMA,
 115 red), and China Meteorological Administration (CMA, blue). The colour shading represents the sea surface level
 116 anomaly on 13 September, 2014, while the gray arrows illustrate the geostrophic flow field. The numbered blue dots
 117 represent the positions of the five buoy/mooring stations, the green line illustrates the trajectory of Argo 2901469,
 118 and the blue diamond's mark the positions of Argo 2901469 inside the eddy AE2 from 26 August 2014 to 25 October
 119 25, 2014.

120 The daily Sea Level Anomaly (SLA) and geostrophic current data are provided by Archiving,
 121 Validation, and Interpretation of Satellite Data in Oceanography (AVISO) product (CMEMS,
 122 <https://marine.copernicus.eu/>, last access: 14 February, 2022). This dataset combines satellite data from
 123 Jason-3, Sentinel-3A, HY-2A, Saral/AltiKa, Cryosat-2, Jason-2, Jason-1, T/P, ENVISAT, GFO, and
 124 ERS1/2. The spatial resolution of the product is $1/4^\circ \times 1/4^\circ$. The period from 1 September to 30
 125 September 2014 was used.

126 The daily Sea Surface Temperature (SST) data used in this study is derived from the Advanced Very
 127 High-Resolution Radiometer (AVHRR) product data provided by the National Oceanic and Atmospheric
 128 Administration (NOAA). The data is obtained from the Physical Oceanography Distributed Active
 129 Archive Center (PODAAC) at the NASA Jet Propulsion Laboratory (JPL)
 130 (ftp://podaac.jpl.nasa.gov/documents/dataset_docs/avhrr_pathfinder_sst.html, last access: 16 March,
 131 2022). The spatial resolution of the data is $1/4^\circ \times 1/4^\circ$.

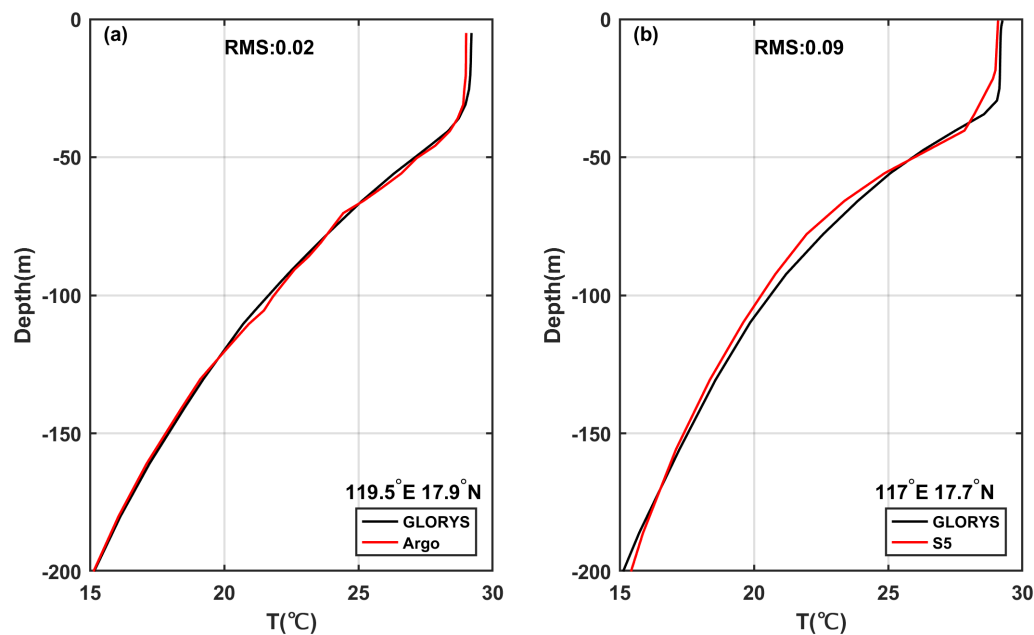
132 Argo data, including profiles of temperature and salinity from surface to 2000 m depth are obtained
 133 from the real-time quality-controlled Argo data base (Euro-Argo, <https://dataselection.euro-argo.eu/>, last
 134 access: 4 April, 2022). We select Argo float number 2901469, situated in an anticyclonic eddy and in
 135 close proximity to Typhoon Kalmaegi, both before and after the typhoon's passage in 2014. Profiles of
 136 this Argo are also used to validate the vertical distribution of temperature and salinity from
 137 GLORYS12V1.

138 For this study, we also utilize in-situ data from a cross-shaped array consisting of five stations,
139 comprising five moored buoys and four subsurface moorings (refer to Fig. 1). More specific information
140 can be found in Zhang et al. (2016). To investigate the impact of the typhoon on a warm eddy, we select
141 the temperature and salinity data from Station 5, situated to the left of Kalmaegi's track.

142 The wind speed data is sourced from the European Centre for Medium-Range Weather Forecasts
143 (ECMWF) ERA-Interim reanalysis assimilation dataset ([https://apps.ecmwf.int/datasets/data/interim-
144 full-daily/levtype=sfc/](https://apps.ecmwf.int/datasets/data/interim-full-daily/levtype=sfc/), last access: 5 January, 2023). We used the reanalysis data of surface winds at a
145 height of 10 meters above sea level for TCs. The selected data has a spatial resolution of $1/4^\circ \times 1/4^\circ$ and
146 a temporal resolution of 6 hours, with four updates per day (00:00, 06:00, 12:00, and 18:00 UTC). The
147 data corresponds to September 2014.

148 The Global Ocean Reanalysis Product GLOBAL_MULTIYEAR_PHY_001_030 (GLORYS12V1),
149 provides by the Copernicus Marine Environment Monitoring Service (CMEMS,
150 <https://marine.copernicus.eu/>, last access: 23 March, 2022) is used in this study too. This reanalysis
151 product utilized the NEMO 3.1 numerical model coupled with the LIM2 sea ice model, and forced with
152 ERA-Interim atmospheric data. The model assimilated along-track altimeter data from satellite
153 observations (Pujol et al., 2016), satellite sea surface temperature data from AVHRR, sea ice
154 concentration from CERSAT (Ezraty et al., 2007), and vertical profiles of temperature and salinity from
155 the CORAv4.1 database (Cabanes et al., 2012). The temperature and salinity biases were corrected using
156 a 3D-VAR scheme. The horizontal resolution is $1/12^\circ \times 1/12^\circ$, and it has 50 vertical levels. The
157 temperature and salinity from 1 September to 30 September 2014 were chosen.

158 GLORYS12V1 is a widely used and applicable dataset, to evaluate its temperature profiles, the Argo
159 profiles and in-situ data of Station 5 were compared (Fig. 2). The GLORYS12V1 data exhibit good
160 agreement with Argo profiling floats, the maximum difference between them is less than 0.2°C , the Root
161 Mean Square (RMS) is 0.02. However, there are some discrepancies between the GLORYS12V1 and
162 the Station 5 data, with the largest difference occurring at the depths of 30 m (mixed layer) and 78 m
163 (thermocline), both differing by 0.6°C , while below 150 m, the difference is quite small. The RMS is
164 0.09. The RMS between GLORYS12V1 and Station 2 (Station 4) is 0.14 (0.10) (Figures not shown).
165 Because the GLORYS12V1 assimilates Argo data and the vertical resolution of Argo profile above 100m
166 is 5 m, but the vertical interval of buoy array is 20 m. Therefore, the large deviations exist at mixed layer
167 and thermocline during the typhoon in in-situ data of Station 5. Overall, GLORYS12V1 reproduces the
168 observed ocean temperature accurately, it is reasonable to use it to investigate the vertical response of
169 anticyclonic eddies to Typhoon Kalmaegi.



171 **Figure 2.** Evaluation of GLORYS12V1 data performance during September 2014. **(a)** Vertical monthly mean
 172 temperature within the anticyclonic eddy AE2 (119.5°E 17.9°N) as measured by Argo float 2901469. **(b)**
 173 Comparison of vertical monthly mean temperature recorded at Station 5 (117°E 17.7°N).

174 2.2. Methods

175 Vorticity is a vector that characterizes the local rotation within a fluid flow. Mathematically, it is
 176 defined as the curl of the velocity vector. In most cases, when referring to vorticity, it specifically pertains
 177 to the vertical component of the vorticity. It is calculated from:

$$178 \quad \zeta = \frac{\partial v}{\partial x} - \frac{\partial u}{\partial y} . \quad (1)$$

179 u and v are the zonal (eastward) and meridional (northward) geostrophic velocities, respectively. They
 180 are derived from altimeter sea level anomaly data (η):

$$181 \quad u = -\frac{g}{f} \frac{\partial \eta}{\partial y} , v = \frac{g}{f} \frac{\partial \eta}{\partial x} . \quad (2)$$

182 Here, g is the acceleration of gravity, f is the Coriolis frequency. Vorticity is considered a
 183 fundamental characteristic of mesoscale eddies, positive vorticity signifies cyclonic eddies, while
 184 negative vorticity indicates anticyclonic eddies.

185 The Rossby number (R_o) is a dimensionless number describing fluid motion, and it is the ratio of
 186 relative vorticity to planetary vorticity, reflecting the relative importance of local non-geostrophic motion
 187 versus large-scale geostrophic motion. The larger the Rossby number, the stronger the local non-
 188 geostrophic effect, and the definition of this parameter is:

$$189 \quad R_o = \frac{\zeta}{f} . \quad (3)$$

190 Eddy Kinetic Energy (EKE) is a measure of the energy associated with mesoscale eddies, which
 191 indicates the intensity of eddies. It is typically calculated using the anomalies of the geostrophic velocity:

$$192 \quad EKE = \frac{1}{2}(u'^2 + v'^2) , \quad (4)$$

193 where u' represents the anomaly of the geostrophic zonal (eastward) velocity, v' represents the anomaly
 194 of the meridional (northward) velocity.

195 To evaluate the impact of a typhoon on an anticyclonic eddy, the calculation begins with determining
 196 the wind stress:

$$197 \quad \vec{\tau} = \rho_a C_d U_{10} \vec{U}_{10} , \quad (5)$$

198 where ρ_a is the air density, assumed to be a constant value of 1.293 kg m^{-3} , U_{10} represents the 10-
 199 meter wind speed. And C_d is the drag coefficient at the sea surface (Oey et al., 2006):

$$200 \quad C_d \times 1000 = \begin{cases} 1.2 & U_{10} \leq 10m \text{ s}^{-1} \\ 0.49 + 0.65U_{10} & 11 \leq U_{10} < 19m \text{ s}^{-1} \\ 1.364 + 0.234U_{10} - 0.00023158U_{10}^2 & 19 \leq U_{10} \leq 100m \text{ s}^{-1} \end{cases} . \quad (6)$$

201 The wind stress curl is calculated by (Kessler, 2006):

$$202 \quad curl(\vec{\tau}) = \frac{\partial \tau_y}{\partial x} - \frac{\partial \tau_x}{\partial y} , \quad (7)$$

203 where τ_x and τ_y are the eastward and northward wind stress vector components, respectively. The curl
 204 represents the rotation experienced by a vertical air column in response to spatial variations in the wind
 205 field.

206 The Ekman pumping velocity (EPV) represents the ocean upwelling rate, which can be used to study
 207 the contribution of typhoons to regional ocean upwelling. Positive means upwelling, negative represents
 208 downwelling:

$$209 \quad EPV = curl\left(\frac{\vec{\tau}}{\rho f}\right) , \quad (8)$$

210 where the wind stress is obtained from Eq. (7), ρ is seawater density, the value is 1025 kg m^{-3} , and f
 211 is the Coriolis frequency.

212 The buoyancy frequency is a measure of the degree to which water is mixed and stratified. In a stable
 213 temperature stratification, the fluid particles move in the vertical direction after being disturbed, and the
 214 combined action of gravity and buoyancy always makes them return to the equilibrium position and
 215 oscillate due to inertia. When $N^2 < 0$, the water is in an unstable state:

$$216 \quad N^2 = -\frac{g}{\rho} \frac{\partial \rho}{\partial z} \quad (9)$$

217 where ρ is seawater density, g is the acceleration of gravity, and z is the depth.

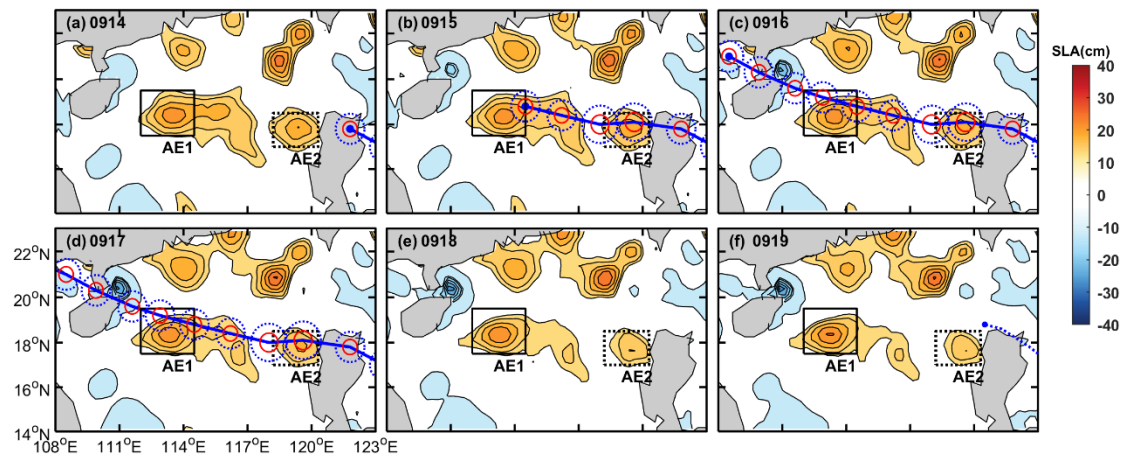
218 **3. Results**

219 **3.1. Typhoon and pre-existing eddies in the NSCS**

220 **3.1.1. Track of Typhoon Kalmaegi and tropical storm Fung-wong**

221 Typhoon Kalmaegi strengthens into a typhoon by 1200 UTC on 13 September and emerged over the
222 warm waters of the Northern South China Sea (NSCS) by 1500 UTC on 14 September, with maximum
223 sustained winds of 33 m s^{-1} (Fig. 3-4). During this period, the NSCS experiences predominantly weak
224 vertical wind shear and is characterized by multiple anticyclonic warm eddies (Fig. 3). Subsequently,
225 Typhoon Kalmaegi undergoes two rapid intensification phases between 15 and 16 September. The first
226 intensification occurs at 0000 UTC on 15 September, propelling Kalmaegi to category 1 status with
227 surface winds surpassing 35 m s^{-1} . By 1200 UTC on 15 September, Kalmaegi experiences a second, even
228 more rapid intensification, with winds reaching 40 m s^{-1} in less than 12 hours. Throughout this
229 intensification stage, Kalmaegi encounters two warm eddies: anticyclonic eddy AE1, is positioned to the
230 left of the typhoon's path, with its core situated on the periphery of the typhoon's two-times maximum
231 wind radius (Fig.3c-d). AE1 has a lifespan of 105 days from 26 June to 8 October and is positioned at
232 17°N - 20°N , 113°E - 116°E . AE2 precisely intersects with the typhoon's trajectory, and its core nearly
233 coincides with the maximum wind radius of the typhoon (Fig.3b-d). It has a lifespan of 89 days from 24
234 August to 20 November and is located at 17°N - 19°N , 118°E - 120°E . Kalmaegi makes landfall on Hainan
235 Island at 0300 UTC on 16 September, with a minimum central pressure of 960 hPa and a maximum wind
236 speed of 40 m s^{-1} . After landfall, Typhoon Kalmaegi gradually weakens and dissipates. During its
237 crossing of the NSCS, the five mooring stations are affected. Stations 1 and 4 are on the right side of
238 Typhoon Kalmaegi's track, while Stations 2 and 5 are on the left side. Unfortunately, the wire rope of the
239 buoy at Station 3 is destroyed by Kalmaegi, resulting in missing data from 15 September. Among the
240 stations, Station 5 is on the left of typhoon track and outside AE2, so its data is used in our study.

241 Tropical storm Fung-wong initially moves quickly in a northwest direction after formation. On 19
242 September, it enters the Luzon Strait and decelerates. It makes landfall in Taiwan on the 21 September
243 and subsequently lands in Zhejiang on the 22 September before gradually dissipating. When crossing the
244 Luzon Strait at 1200 UTC on 19 September, anticyclonic eddy AE2 is on the left side of Fung-wong,
245 with a distance of just over 100 km from its center.



247 **Figure 3.** The variations in sea level anomaly before and after Typhoon Kalmaegi moved over the anticyclonic eddies
 248 AE1 and AE2 between 14 September and 19 September (a-f). The black solid rectangle represents the area of AE1,
 249 while the black dashed rectangle represents the area of AE2. The blue solid line depicts the path of Typhoon
 250 Kalmaegi, the solid red and dashed blue circles are the one- and two-times maximum wind radius of the typhoon,
 251 while the blue dotted line in (f) is the path of tropical storm Fung-wong (best-track data sourced from CMA).

252 3.1.2. Eddy characteristics distribution

253 Satellite SLA measurements have proven to be highly effective and widely used for identifying and
 254 quantifying the intensity of ocean eddies (Li et al., 2014). In Fig. 3, two warm eddies with clear positive
 255 (> 13 cm) SLA are observed along the Typhoon Kalmaegi's track. During the period of 15 to 16
 256 September, the typhoon passes over two warm anticyclonic eddies, AE1 and AE2. Before the typhoon,
 257 AE1 is the most prominent eddy in the SCS, with an amplitude of 23.0 cm, and a radius of 115.5 km.
 258 AE2, located west of Luzon Island, has an amplitude of 21.2 cm, with a radius of approximately 65.5
 259 km. Tracing back to 2 months (figure is not shown), AE1 propagates slowly westward with about 0.1 m s^{-1} ,
 260 while AE2 is generated on 24 August. During 14 to 19 September, the amplitude of AE1 increases
 261 1.3 cm. The area of the AE1 decreases by approximately 31% from $1.3 \times 10^5 \text{ km}^2$ to $9.1 \times 10^4 \text{ km}^2$ and
 262 splits into two eddies. When Typhoon Kalmaegi crosses the core of AE2 at 1500 UTC on 14 September,
 263 and tropical storm Fung-wong moves over the northeast of AE2 at 1200 UTC on 19 September, the
 264 amplitude decreases by 3.1 cm. The area of the AE2 decreases by approximately 36% from $4.2 \times 10^4 \text{ km}^2$
 265 to $2.7 \times 10^4 \text{ km}^2$.

266 Because of intense solar radiation in September, the SST in the SCS is generally above 28.5°C prior
 267 to the arrival of Typhoon Kalmaegi (Fig. 4a). As a fast-moving typhoon with a mean moving speed of
 268 over 8 m s^{-1} , Kalmaegi induces a larger cooling area and intensity on the right side of its path compared
 269 to the left side (Price, 1981). During the passage of Kalmaegi, the lowest SST on the right side of typhoon
 270 decreases to 27.2°C . Even after the typhoon has passed, a cold wake could still be observed on the right
 271 side of its path, persisting for over a week (Fig. 4c).

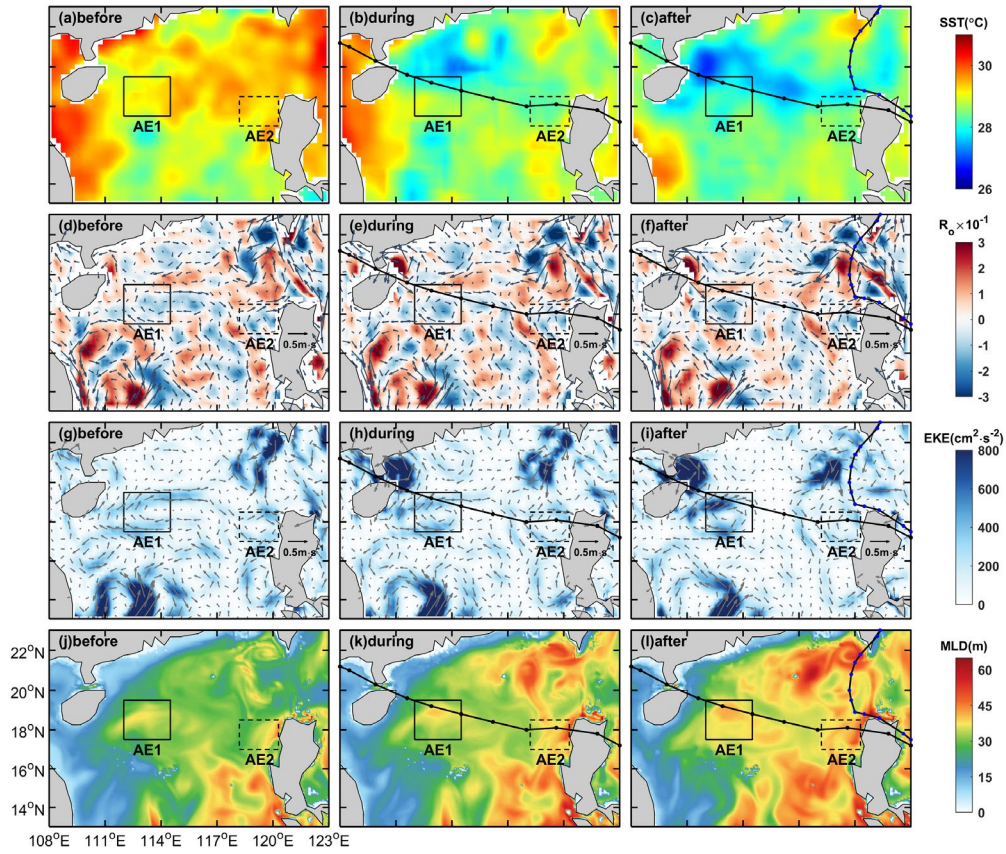
272 The pre-existing warm eddy AE1 begins to cool down before Kalmaegi reached the NSCS, dropping
 273 to 28.4°C on 14 September. During this period, the mean SST within AE1 increases slightly to 28.6°C
 274 (Fig. 5a). However, as cooler water from the right side of the typhoon track is subsequently advected into

275 the AE1 region (Fig. 4c), the SST decreases and reaches 28.0 °C on September 19, which is 0.4°C lower
276 than that before the typhoon. The average SST drop in AE2 is evident, with SST starting to decline before
277 14 September and reaching its lowest temperature (28.1°C) on 15 September, 0.6 °C lower than that
278 before the typhoon (Fig. 5e). On 16 September, the SST within AE2 begins to recover, but it starts to
279 cool again on 18 September due to the influence of Fung-wong.

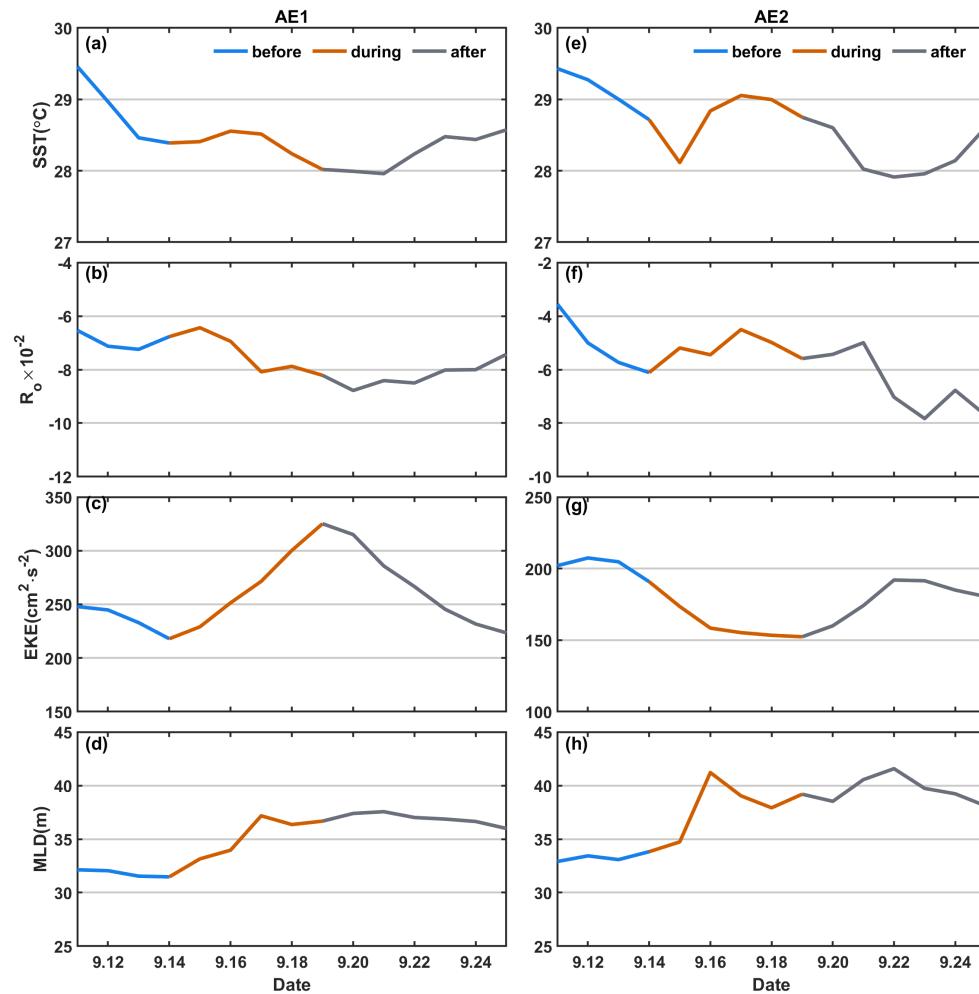
280 Then we compare the R_o and EKE of AE1 and AE2 before, during and after typhoon. Before being
281 influenced by the typhoon, the warm eddy AE1 exhibits a more scattered distribution of negative R_o due
282 to its edge structure, and the EKE values at the eddy boundary are relatively high (Fig. 4d, g). As the
283 typhoon passes through the eddy, the R_o and EKE of AE1 increase. On 19 September, the average R_o
284 within AE1 reaches a value of -8.2×10^{-2} , at the same time, the average EKE increases to its maximum
285 value of $325.0 \text{ cm}^2 \text{ s}^{-2}$. The variation trend of R_o and EKE within the eddy is consistent, increasing from
286 the passage of the typhoon and starting to recover on 20 September (Fig. 5b-c). This indicates that
287 although the area of the warm eddy AE1 decreased under the influence of the typhoon, its intensity
288 increases. On the other hand, for warm eddy AE2, both R_o and EKE decreases after the typhoon passage,
289 with the R_o decreasing to -4.5×10^{-2} on 17 September and the EKE decreasing to $152.0 \text{ cm}^2 \text{ s}^{-2}$ on the 19
290 September, following by a recovery (Fig. 5f-g). Unlike AE1, AE2 weakens in intensity under the
291 influence of the typhoon.

292 During the passage of the typhoon, wind stress-driven mixing enhancement and an increase in vertical
293 shear result a deepening of the MLD, which further strengthens the mixing between the deep cold water
294 and the upper warm water (Shay and Jaimes, 2009). To avoid a large part of the strong diurnal cycle in
295 the top few meters of the ocean, 10 m is set as the reference depth (De Boyer Montégut, 2004). A 0.5 °C
296 threshold difference from 10 m depth is calculated and defined as the MLD (Thompson and Tkalich,
297 2014). Prior to the influence of typhoon Kalmaegi, the MLD in the AE1 and AE2 regions is deeper (Fig.
298 4j), with the average MLDs of 32 m and 33 m, respectively. Starting from 14 September, the MLDs are
299 influenced by typhoon Kalmaegi, with the MLD of AE1 deepening to 37 m and that of AE2 increasing
300 to 41 m, representing a deepening of 5 m and 8 m, respectively (Fig. 5d, h).

301 Overall, Typhoon Kalmaegi likely exerts distinct impacts on the two warm eddies. Despite both AE1
302 and AE2 experiencing a decrease in their respective areas by approximately one-third, accompanied by
303 deepening of the MLD, the amplitude of SLA within AE1 increases by 1.3 cm, whereas AE2 witnesses
304 a decrease of about 3.1 cm in its amplitude. Furthermore, the SST, Rossby number and EKE within AE1
305 and AE2 exhibited contrasting patterns.



307 **Figure 4.** The spatial distribution of SST, R_o , EKE, and MLD before, during and after the passage of TCs. The
 308 time periods of 10-13, 15-16 and 19-22 September are designated as stages before, during and after Kalmaegi,
 309 respectively. The path of Typhoon Kalmaegi is depicted by a black solid line with black dots, while the path of
 310 tropical storm Fung-wong is represented by a black solid line with blue dots in the third column. The solid and
 311 dashed boxes correspond to AE1 and AE2, respectively.



313 **Figure 5.** The time series of sea surface temperature (SST), R_0 , eddy kinetic energy, and mixed layer depth (MLD)
 314 within the warm eddies' regions (black solid and dashed boxes in Fig. 4). The first column is variables of AE1, the
 315 second column is for AE2.

316 3.2 Upper-ocean vertical thermal and salinity structure of eddies

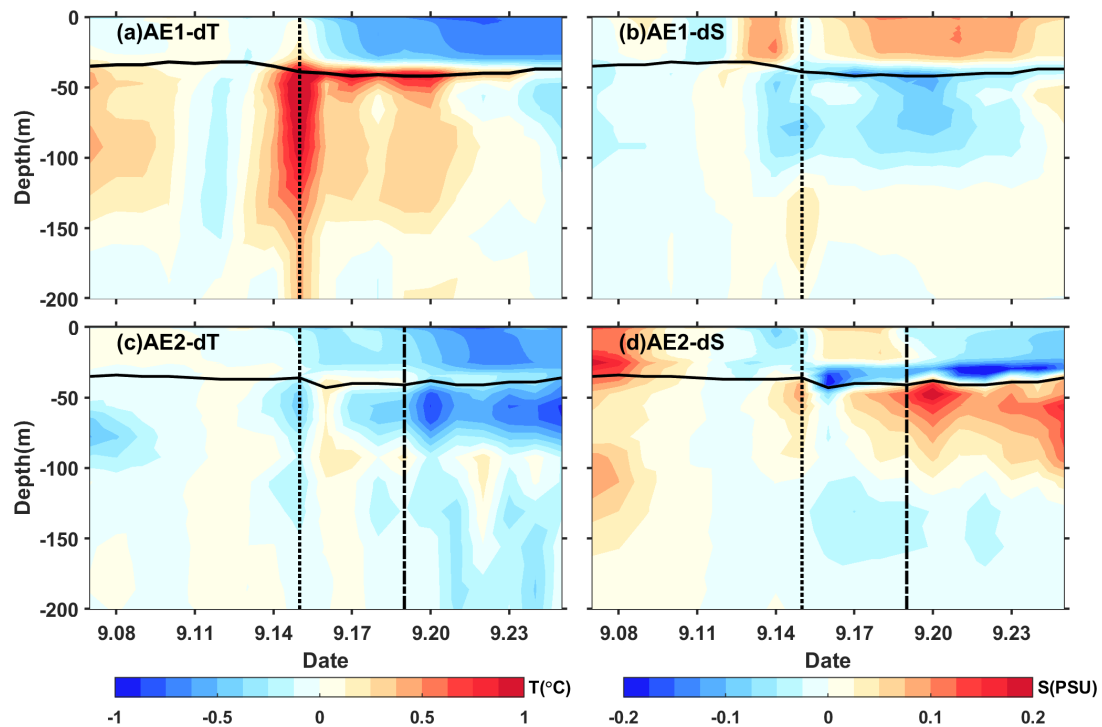
317 We conducted further analysis on the vertical temperature and salinity structure of the warm eddies
 318 AE1 and AE2 before and after the Typhoon Kalmaegi using GLORYS12V1 data. During the typhoon's
 319 passage on 15 September, the temperature above the MLD within AE1 increases by approximately 0.1 °C,
 320 while the salinity decreases by 0.02psu (Fig. 6). Below the MLD, the temperature shows a significant
 321 increase, reaching a maximum temperature rise of 1.3 °C. Correspondingly, the salinity below the MLD
 322 exhibits a decrease of 0.05 psu. Vertical temperature on Kalmaegi's arrival day shows warm pattern from
 323 surface to 200 m, the salinity shows "fresher-saltier" pattern. These changes lead to a deepening of
 324 isopycnals by 15 m and a decrease in buoyancy frequency N^2 (Fig. 7a-b), indicating convergence and
 325 downwelling within the centre of the warm eddy AE1. The near-inertial waves propagates downward
 326 from surface to 200m during this period (Zhang et al, 2017). The transfer of energy from anticyclonic
 327 eddy to near-inertial waves is the main reason for the downward propagation and longtime persistence
 328 of near-inertial energy (Chen et al, 2023).

329 After 15 September, the temperature above the MLD decreases, and the salinity shows an increase
 330 (Fig. 6a-b), resulting in the uplift of the 1021 kg m^{-3} isopycnal to the sea surface (Fig. 7a-b). The
 331 subsurface warming and salinity reduction gradually weakens after the Typhoon Kalmaegi but persists
 332 for about a week after the typhoon's passage until 22 September. During this period, vertical temperature
 333 pattern becomes "cool-warm" at the center of AE1, and the salinity distribution pattern becomes "saltier-
 334 fresher-saltier". This persistence can be attributed to the intensified stratification around the MLD, with
 335 N^2 around $9.0 \times 10^{-4} \text{ s}^{-2}$ (Fig. 7b). The increased stability inhibits vertical mixing, restrains the exchange
 336 of heat and salinity, and leads to smoother density gradients above the MLD (Fig. 7a).

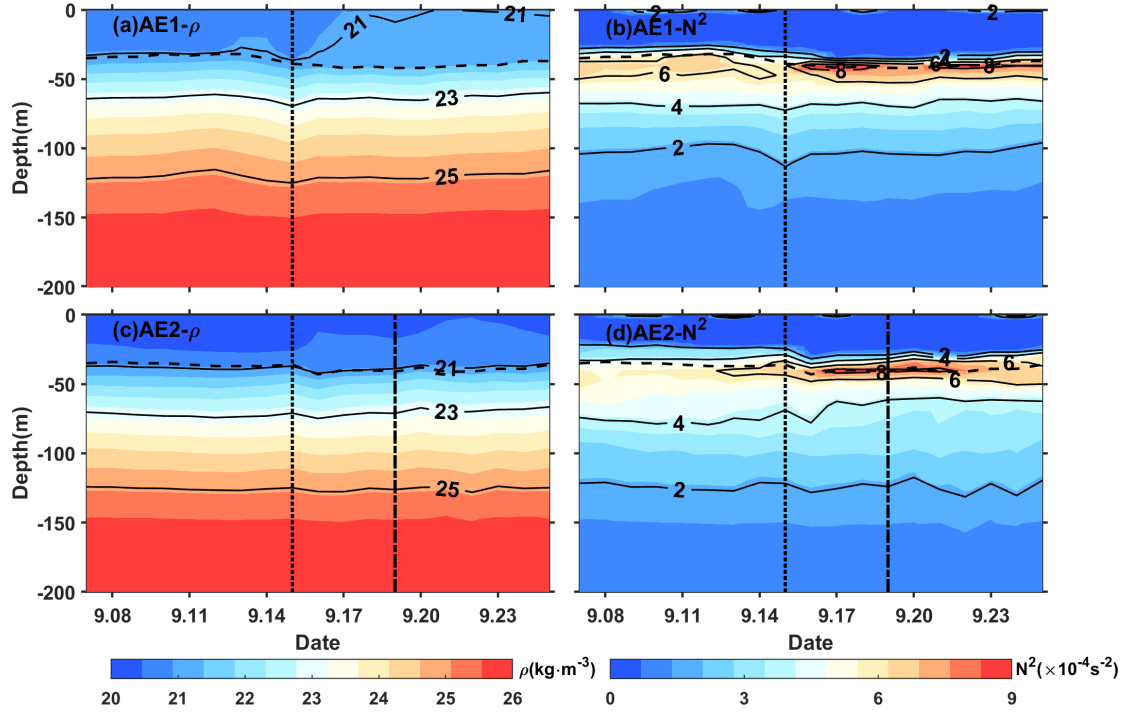
337 The vertical temperature and salinity structure of AE2 exhibits an opposite trend. During the typhoon
 338 passage on 15 September, AE2 also experiences a cooling trend of $0.2 \text{ }^\circ\text{C}$, with a decrease in salinity of
 339 0.04 psu above the MLD. Below the MLD, the temperature shows a consistent decrease, with a change
 340 of less than $0.5 \text{ }^\circ\text{C}$ within the subsurface. Correspondingly, the salinity exhibits an increase of
 341 approximately 0.08 psu (Fig. 6c-d). The slightly upward shift of the isopycnals (Fig. 7c) suggests the
 342 possibility of cold-water upwelling induced by the suction effect of the typhoon. The temperature
 343 decreases and salinity increases below the MLD are primarily driven by upwelling.

344 Furthermore, when the tropical storm Fung-wong passes through AE2 on 19 September (dashed line
 345 in Fig. 6c-d), the decreasing trend of subsurface temperature becomes more pronounced, and the
 346 subsurface salinity exhibits a significant increase. AE2 is more significantly influenced by tropical storm
 347 Fung-wong. It presents stable stratification with N^2 around $8.4 \times 10^{-4} \text{ s}^{-2}$ at a depth of 42 m , creating a
 348 barrier layer that prevents the intrusion of high-salinity cold water from the lower layers into the mixed
 349 layer (Yan et al., 2017).

350



352 **Figure 6.** The timeseries of vertical temperature and salinity anomalies in the center of AE1(a,b) and AE2 (c,d).
 353 The anomalies were calculated relative to the average value of 10-13 September. The vertical black dotted line
 354 indicates the Typhoon Kalmaegi's passage, while the vertical black dashed line represents the passage of tropical
 355 storm Fung-wong. The black solid line is the MLD.



357 **Figure 7.** Same as Fig. 7, but for density and buoyancy frequency (N^2).

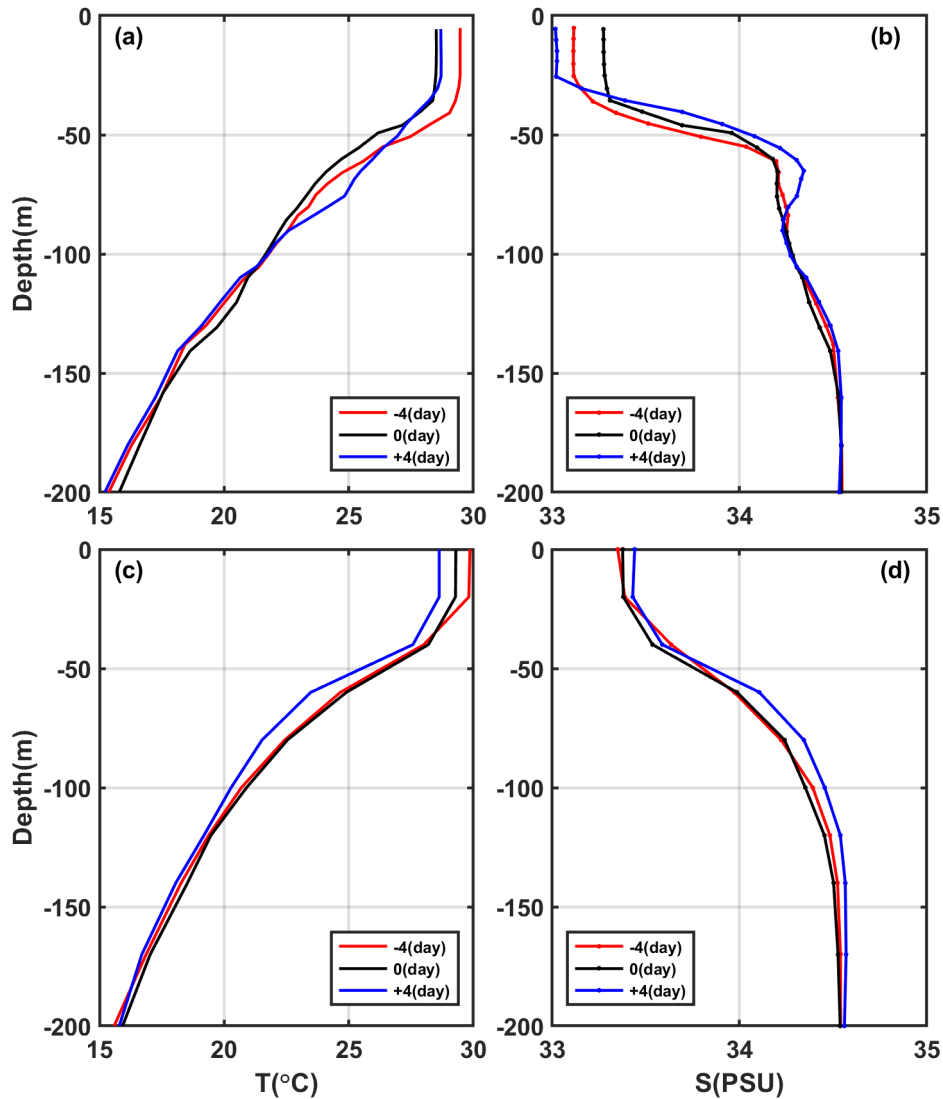
358 3.3 Comparison of the response between eddies and non-eddies areas

359 To investigate the contrasting response of warm eddies and the non-eddies background to Typhoon
 360 Kalmaegi, we conduct a comparative analysis of vertical temperature and salinity profiles in these two
 361 areas. Unfortunately, there is no Argo data around AE1, therefore, we examine data from Argo 2901469,
 362 which is located within AE2 during the period from 11 to 19 September. The temperature and salinity
 363 data from Station S5 is considered as the background, with S5 located at a distance of 246 km from
 364 AE2's center on 15 September (Fig. 1). These profiles are categorized into three periods: pre-typhoon
 365 (11 September), during-typhoon (15 September), and post-typhoon (19 September).

366 At depths above 40m, both the inside and outside of AE2 experience a decrease in temperature, with
 367 a cooling of less than -1.0°C . Four days after the typhoon passage (19 September), the cooling persists
 368 inside and outside the eddy, with the cooling being more pronounced outside AE2, showing a decrease
 369 of 1.2°C (Fig. 8c). The salinity within AE2 initially increases by 0.15 psu from the pre-typhoon stage to
 370 the during-typhoon stage and then decreases by 0.09 psu after the typhoon passage (Fig. 8d). While the
 371 salinity at Station 5 shows a similar pattern in pre-typhoon and during-typhoon stage, it increases by 0.05
 372 psu after the typhoon. Two possible processes can explain the difference in salinity trends inside and
 373 outside AE2. First, during the pre-typhoon to typhoon stage, the entrainment within AE2 may have
 374 brought the subsurface water, which is saltier, up to the surface, resulting in an increase in salinity. The

375 second process is related to the typhoon-induced precipitation after the typhoon passage, which lead to a
376 decrease in salinity. Strong stratification has contributed to the persistence of saltier subsurface water.
377 While at S5, the increase in salinity is relatively minor.

378 On 15 September, the subsurface layer at 45 m to 100 m is affected by the cold upwelling, which is
379 caused by the typhoon, resulting in a cooling and increased salinity within AE2. As the forcing of
380 Typhoon Kalmaegi diminishes, the upper layer of seawater begins to mix, and warm surface water is
381 transported to the subsurface layer. Four days later, a warming phenomenon occurs, with the maximum
382 warm anomaly of 1.2 °C observed at a depth of 75 m (Fig. 8a). The mixing effect outside the eddy is not
383 significant, resulting in a slight subsurface warming of approximately 0.2 °C, with no significant changes
384 in salinity. However, on 19 September, a maximum cold anomaly of -1.2°C is observed at depth of 60
385 m, corresponding to the maximum salinity anomaly of 0.13 psu (Fig. 8c-d). Below 100 m, AE2
386 experiences a temperature increase of 0.5 °C and a slight decrease in salinity of 0.04 psu. On 19
387 September, the temperature and salinity within AE2 show little change. However, outside the eddy, a
388 different response is observed. On 19 September, a cooling trend is observed throughout the water
389 column, within a range of 0.2 °C, accompanied by a noticeable increase in salinity (Fig. 8c, d), within a
390 range of 0.06 psu. This indicates that the typhoon causes a significant upwelling outside the eddy region.



392 **Figure 8.** (a-b) the vertical profile of temperature and salt inside the eddy (Argo 2901469), (c-d) the vertical profiles
 393 of temperature and salt outside the eddy (S5). The red, black and blue lines represent pre-typhoon, during-typhoon
 394 and post-typhoon stages.

395 Based on Argo profiles and S5 data, the upper ocean above 200 m inside and outside AE2 responds
 396 differently to the forcing of the typhoon. In the upper layer (0-40 m), cooling is observed both inside and
 397 outside the eddy, and it lasts longer. In the subsurface layer (45-100m), after the passage of the typhoon
 398 (19 September), there is a strong cooling outside the eddy, while warming occurs within AE2. Zhang
 399 (2022) points out that the sea temperature anomalies mainly depend on the combined effects of mixing
 400 and vertical advection (cold suction). Mixing causes surface cooling and subsurface warming, while
 401 upwelling (downwelling) leads to cooling (warming) of the entire upper ocean. The temperature anomaly
 402 in the subsurface layer depends on the relative strength of mixing and vertical advection, with cold
 403 anomalies dominating when upwelling is strong, and downwelling amplifying the warming anomalies
 404 caused by mixing. Therefore, due to the strong influence of upwelling outside the eddy, the temperature
 405 profile of the entire water column shifts upwards, resulting in cooling of the entire upper ocean. On the
 406 other hand, influenced by the downwelling associated with the warm eddy itself, a warming anomaly of

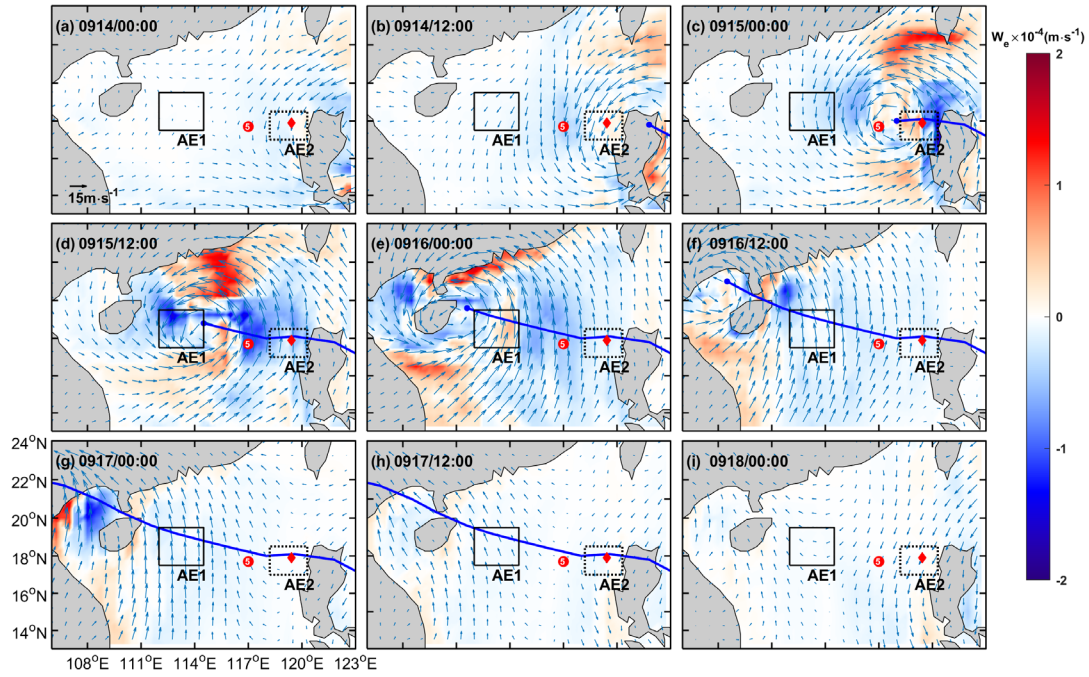
407 1.2 °C is observed in the subsurface layer. Compared to region AE2, the cold suction effect caused by
408 the Typhoon Kalmaegi is still evident in the non-eddy area.

409 In the following sections, we delve into the underlying reasons behind these different responses of
410 AE1 and AE2 to Typhoon Kalmaegi.

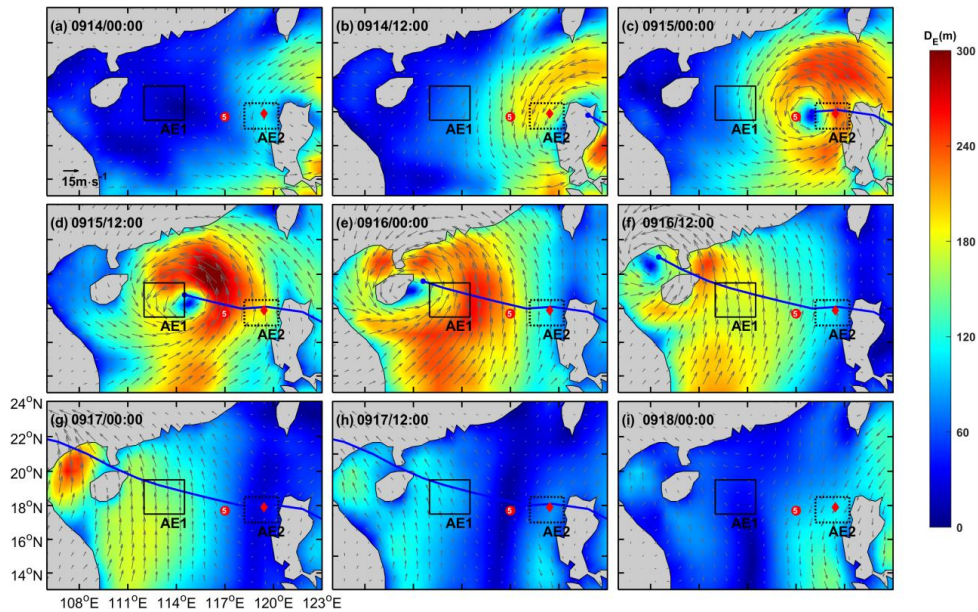
411 **4. Discussion**

412 The EPV is very small before the typhoon, measuring less than $0.5 \times 10^{-5} \text{ m s}^{-1}$ in both AE1 and AE2.
413 However, during 15-16 September (Fig. 9c-f), when typhoon crosses the NSCS, the EPV undergoes
414 significant changes. Its absolute value increases to over $1.5 \times 10^{-4} \text{ m s}^{-1}$ within both AE1 and AE2. AE1
415 consistently exhibits a predominantly negative EPV during most of this period. Consequently, during
416 Typhoon Kalmaegi, the negative EPV facilitates downwelling and convergence (Jaimes and Shay, 2015),
417 leading to a warmer and fresher subsurface layer in AE1 (Fig. 6 a-b).

418 On the other hand, AE2 displays a more fluctuating pattern. It is positive on 14 September, shows
419 both positive and negative values at 0000 UTC on 15 September, and remains mainly negative from 15
420 to 16 September, and eventually returning to positive, reflecting a continuously fluctuating process. The
421 positive EPV in AE2 contributes to the influx of colder subsurface water into the upper layers, resulting
422 in surface and subsurface water cooling and an increase in salinity in the subsurface (Fig. 6c-d).
423 Correspondingly, the variations in Ekman layer depth (D_E) with the typhoon's passage are similar to EPV,
424 as shown in Fig. 10. When Kalmaegi approaches at 0000 UTC on 14 September, the mean D_E within
425 AE1 is only 21 m, while in AE2, it is 114 m. This indicates that AE2 has already been influenced by
426 Typhoon Kalmaegi. Subsequently, the depth of the DE within AE2 sharply deepens, reaching its
427 maximum depth of 241 m at 0000 UTC on 15 September, coinciding with the proximity of Typhoon
428 Kalmaegi's center to AE2. As Kalmaegi moves northwest, the D_E within AE1 achieves its maximum
429 depth of 262 m at 0000 UTC on 16 September. The trends of D_E within AE1 and AE2 are nearly
430 consistent, but AE1 lags behind AE2 by one day. Starting from 15 September, D_E within both AE1 and
431 AE2 gradually shallows, reaching a minimum D_E of 60 m. This value is 28 m higher than before the
432 typhoon, indicating the lingering effects of the typhoon through wind. For AE2, D_E reached its minimum
433 of 45 m at 0000 UTC on 18 September, later gradually increasing under the influence of tropical storm
434 Fung-wong.



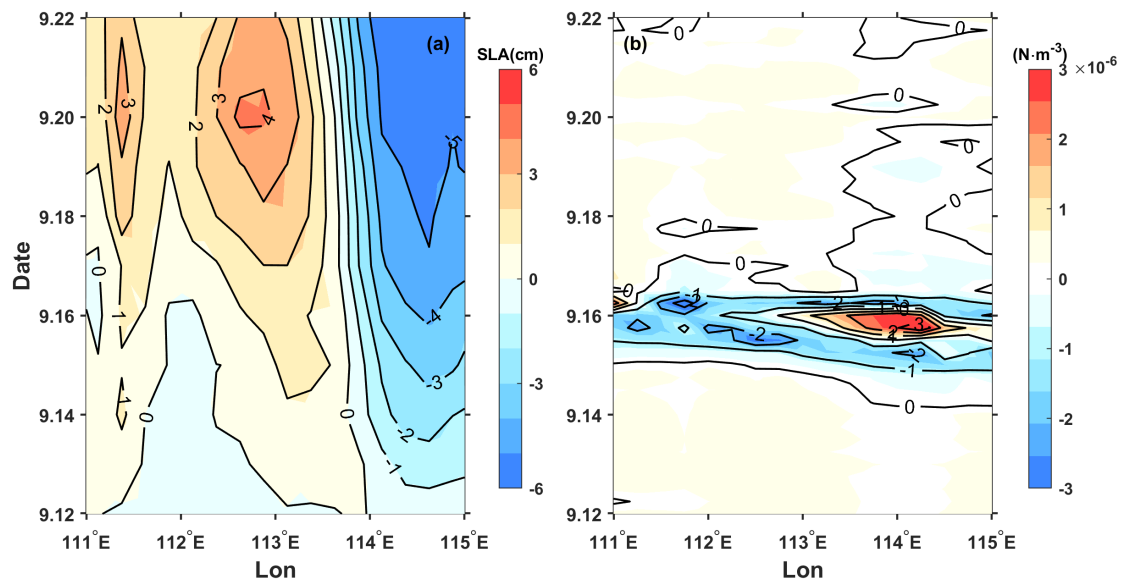
436 **Figure 9.** Ekman Pumping Velocity (EPV) from 14 September to 18 September (a-i). The color represents the EPV,
 437 the blue solid line is the path of Kalmaegi, the red dot and diamond are the positions of Station 5 and Argo 2901469
 438 on 15 September, respectively.



440 **Figure 10.** Ekman layer depth (D_E) from 14 September to 18 September (a-i). The color represents the D_E , the blue
 441 solid line is the path of Kalmaegi, the red dot and diamond are the positions of Station 5 and Argo 2901469 on 15
 442 September, respectively.

443 After traversing the warm ocean characteristics of AE2, Typhoon Kalmaegi strengthens, resulting in
 444 a reduction of the maximum wind radius. As it passed through AE1, the maximum wind radius is 35 km.
 445 Notably, the center of AE1 is located outside the typhoon's two-times maximum wind radius,
 446 approximately 104 km away from the typhoon center (Fig. 3). As mentioned earlier, strong upwelling
 447 occurs within two-times maximum wind radius, while weak subsidence exists in the vast area outside

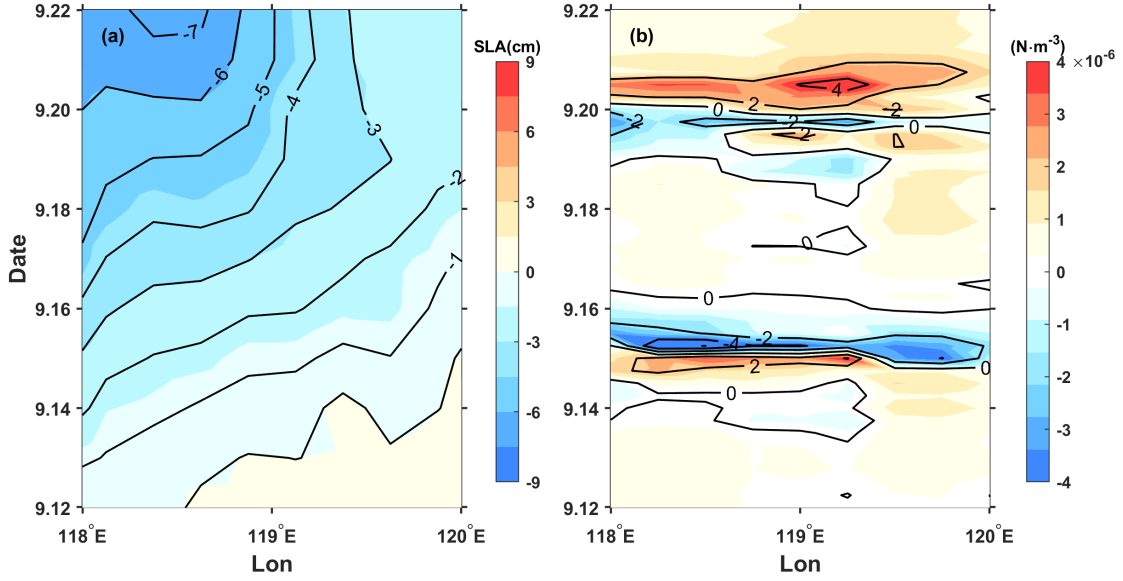
448 the upwelling region (Jaimes and Shay, 2015). Hence, the hypothesis presented here suggests that the
 449 observed intensification of AE1 on the left side of the typhoon track is more likely attributed to the
 450 negative wind stress generated outside the maximum wind radius, driving the enhancement of
 451 downwelling in the pre-existing anticyclonic feature in the ocean. Starting from 15 September, a
 452 significant positive sea level anomaly (SLA) to the west of 113.5°E becomes evident, intensifying and
 453 reaching its maximum on 20 September (Fig. 11a). This strengthening aligns with the increase in the
 454 amplitude of the warm core of the eddy AE1. A comparison with the wind stress curl anomaly (Fig. 11b)
 455 reveals that between 15 to 16 September, as the Typhoon Kalmaegi moves over the section at 18.2°N,
 456 specifically to the west of 113.5°E, it exhibits strong negative wind stress curl anomalies, with a
 457 maximum intensity of $-3 \times 10^{-6} \text{ N m}^{-3}$. The negative wind stress curl induced by the typhoon results in
 458 favourable surface ocean currents that further enhances the clockwise rotation of the warm eddy. The
 459 negative wind stress curl anomaly results in strong downwelling currents, inputting negative vorticity
 460 into AE1, leading to its intensification (Fig. 4b-c), as indicated by the enhanced positive SLA (Fig. 11a).
 461 Conversely, the region to the east of 113.5°E along the section exhibited negative SLA anomalies. This
 462 weakening is consistent with the previous observations of the intensified warm core and decreased eddy
 463 area.



465 **Figure 11.** The time/longitude plots of (a) SLA anomaly (cm) and (b) wind stress curl (N m^{-3}) anomaly at the central
 466 section of AE1 (18.2°N). The anomalies were calculated relative to the average value of 10-13 September.

467 The response of AE2 differs from that of AE1 mainly because AE2 is quite near the Typhoon
 468 Kalmaegi's track. As the typhoon passes through AE2, the maximum wind radius is 48 km. AE2 is
 469 merely 26 km away from the typhoon center (Fig. 3). The significantly positive wind stress curl at the
 470 typhoon center induces upwelling and positive vorticity downward into the eddy (Huang and Wang,
 471 2022), and noticeably weakens the eddy, corresponding to the decrease in SLA (Fig. 12a). Furthermore,
 472 based on the meridional isotherm profiles of the eddy center at three dates, it can be observed that during
 473 the passage of Typhoon Kalmaegi (15 September), the isotherms in the AE1 region exhibit significant
 474 subsidence (Fig. 13a), while in the AE2 region, the isotherms show uplift (Fig. 13b). This result aligns

475 with the earlier observation that the convergence and subsidence within the warm eddy AE1 are enhanced
 476 by the influence of the wind stress curl induced by the typhoon, while the intensity of AE2 is weakened.



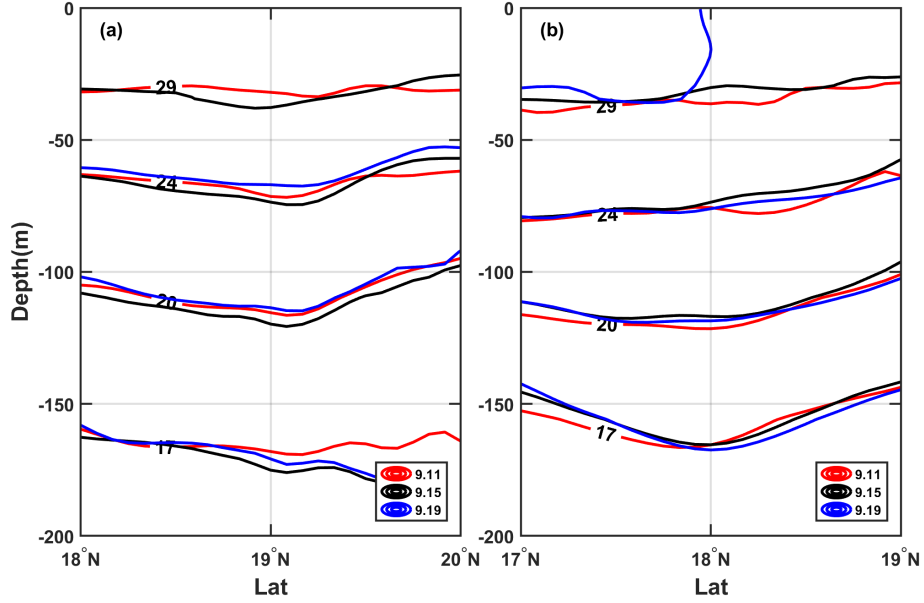
478 **Figure 12.** Same as Fig.10, but for AE2(17.9 °N).

479 From the above, the relative position of eddies and the typhoon can influence the response of the
 480 eddies (Lu et al., 2020). The warm eddy AE1, located on the left side of the typhoon track, is not
 481 weakened by the strong cold suction effect caused by the typhoon Kalmaegi. Instead, it is strengthened
 482 due to the stronger negative wind stress curl generated by the typhoon.

483 To understand the work done by the Typhoon Kalmaegi on the eddies in the ocean, we estimate the
 484 total work inputted into the ocean current u_c using the previously calculated wind stress (Liu et al.,
 485 2017):

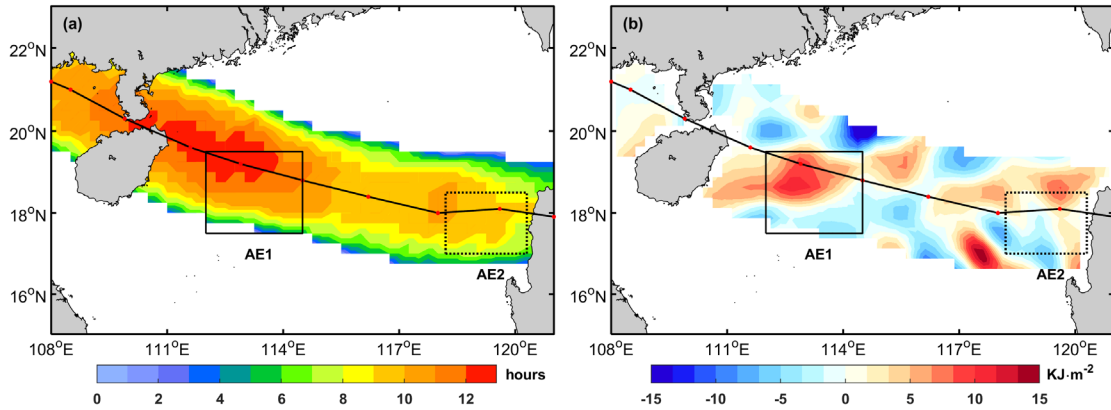
486
$$W = \int \vec{\tau} \cdot \vec{u}_c dt . \quad (10)$$

487 Here, we select the region near the typhoon track where the wind speed exceeds 17 m s^{-1} as the typhoon
 488 forcing region to know the energy input by the typhoon to the warm eddy (Sun et al., 2010). The forcing
 489 duration over the ocean in the typhoon-affected region and the work done by the typhoon on the surface
 490 current are shown in Fig. 14. When the angle between the wind and the ocean current is acute, the typhoon
 491 does positive work on the ocean current. Conversely, when the angle is obtuse, the typhoon does negative
 492 work on the ocean current. It is evident that the region with the maximum forcing duration by the typhoon
 493 on AE1 corresponds to the area where the typhoon clearly does positive work on the ocean current,
 494 accumulating a work done exceeding 8 KJ m^{-2} . This acceleration of the flow velocity in the eddy results
 495 in convergence within the eddy and an increase in SLA, leading to the strengthening of AE1. On the
 496 other hand, the forcing duration by the typhoon on AE2 is smaller, and the typhoon does negative work
 497 on the ocean current in most areas, with a cumulative work done within -5 KJ m^{-2} , causing the flow
 498 velocity within the AE2 to decelerate.



500 **Figure 13.** The meridional isotherm profiles of AE1 (a) and AE2 (b) before (11 September), during (15 September)
 501 and after (19 September) typhoon Kalmaegi.

502



504 **Figure 14.** (a): the forcing time (unit: hours) of the typhoon; (b): the input work (unit: KJ m^{-2}) of the typhoon to
 505 the current.

506 **5. Summary**

507 Based on multi-satellite observations, in situ measurements, and numerical model data, we have
 508 gained valuable insights into the response of warm eddies AE1 and AE2 in the northern South China Sea
 509 to Typhoon Kalmaegi. Both horizontally and vertically, these eddies display distinct differences.
 510 Horizontally, we observe a reduction of areas by approximately 31% (AE1) and 36% (AE2). AE1,
 511 positions on the left side of the typhoon's track, strengthens with amplitude, R_o and EKE increasing by
 512 1.3 cm, 1.4×10^{-2} and $107.2 \text{ cm}^2 \text{ s}^{-2}$ after the typhoon passed. In contrast, AE2, which intersects with the
 513 typhoon's track, weakens with amplitude, R_o and EKE decreasing by 3.1 cm, 1.6×10^{-2} and $38.5 \text{ cm}^2 \text{ s}^{-2}$,
 514 respectively. Vertically, during the typhoon's passage, AE1 experiences intensified converging
 515 subsidence flow at its center, leading to an increase in temperature and a decrease in salinity above 150
 516 m. This response is more pronounced below the MLD (1.3°C) and persists for about a week after the

517 typhoon. On the other hand, AE2 exhibits cooling above the MLD, accompanied by a decrease in salinity,
518 as well as a subsurface temperature drop and salinity increase due to the upwelling of cold water caused
519 by the typhoon's suction effect. The subsurface cooling and salinity increase in AE2 are further
520 influenced by Typhoon Fung-wong. Additionally, from the temperature vertical profile of Argo and in-
521 situ arrays, on 19 September, it can be seen that the non-eddy region also experiences significant cooling,
522 with a prominent cooling center observed at a depth of 60 m (-1.2 °C). The warm eddy AE2, influenced
523 by its own downwelling, exhibits enhanced mixing effects, resulting in a subsurface warm anomaly of
524 1.2 °C.

525 Further analysis reveals that the different responses of the warm eddies can be attributed to factors
526 such as wind stress curl distribution, which are influenced by the relative position of the warm eddies
527 and the typhoon track. The wind stress curl induced by the typhoon plays a crucial role in shaping the
528 response of the warm eddies. AE1, located on the left side of the typhoon's path, experiences prolonged
529 forcing from the typhoon, resulting in positive work on the ocean current. This inputs a strong negative
530 wind stress curl into the eddy, enhancing negative EPV and deepening D_E , so the downwelling within
531 the AE1 is obvious and contributing to its increased strength. In contrast, AE2, positioned directly below
532 the typhoon's track, experiences shorter forcing duration and weakens due to the strong positive wind
533 stress curl at the typhoon's center and shallower D_E . Furthermore, the absolute value of EPV increases in
534 both warm eddies during the typhoon's passage, but with differing impacts. The positive EPV contributes
535 to surface water cooling and the influx of cooler subsurface water, while the negative EPV facilitates
536 downwelling and intensifies the influence of the warm eddies.

537 While numerous prior studies exploring the interaction between TCs and eddies have predominantly
538 drawn generalized conclusions, such as the weakening (strengthening) effect of cold (warm) eddies.
539 Conversely, TCs are recognized for strengthening cold eddies and weakening warm eddies. However,
540 our study takes a different approach. We aim to illustrate that even when TCs encounter eddies of the
541 same polarity, the response of these eddies to TCs exhibits variations. This nuanced response is intricately
542 linked to factors including the relative position of the eddies and the TCs, the eddies' intensity, and the
543 background current. It is discussed first time in the South China Sea. By analyzing wind stress curl
544 distribution, EPV, buoyancy frequency and the relative position between the eddies and the typhoon's
545 track, this case study provides a more nuanced understanding of the mechanisms driving these different
546 eddy-typhoon interactions in the Northern South China Sea. Moreover, it will further improve the
547 accuracy of TC forecasts and enhancing the simulation capabilities of air-sea coupled models.

548
549

550 *Data availability.* The six-hourly best-track typhoon datasets were accessed on 3 February 2021 by JTWC,
551 <http://www.usno.navy.mil/JTWC>, JMA, <https://www.jma.go.jp/jma/jma-eng/jma-center/rsmc-hp-pub-eg/besttrack.html> and CMA, <http://tcdata.typhoon.gov.cn>. The AVISO product was accessed on 14 February
552 2021 by <https://marine.copernicus.eu/>. The AVHRR SST data was accessed on 16 March, 2022 by
553 ftp://podaac.jpl.nasa.gov/documents/dataset_docs/avhrr_pathfinder_sst.html. The Argo data was accessed
554 on 4 April, 2022 by <https://dataselection.euro-argo.eu/>. The wind data was accessed on 5 January, 2023 by

556 <https://apps.ecmwf.int/datasets/data/interim-full-daily/levtype=sfc/>. The GLORYS12V1 was accessed on
557 23 March, 2022 by <https://marine.copernicus.eu/>.

558 *Author contributions.* XYL and HZ contributed to the study conception and design. Material preparation, data
559 collection and analysis were performed by YHH and XYL. GQH and YL contributed to the methodology. The
560 original manuscript was prepared by XYL and YHH. All the authors contributed to the review and editing of
561 the manuscript.

562 *Competing interests.* The contact author has declared that none of the authors has any competing interests.

563 *Disclaimer.* Publisher's note: Copernicus Publications remains neutral with regard to jurisdictional claims in
564 published maps and institutional affiliations.

565 *Acknowledgements.* These data were collected and made freely available by JTCW, JMA, CMA, AVISO, AVHRR,
566 Argo, ECMWF, COPERNICUS. All figures were created using MATLAB, in particular using the M_Map toolbox
567 (Pawlowicz, 2020). The authors thank the anonymous reviewers, whose feedback led to substantial im-
568 provement of the resulting analyses, figures and manuscript

569 *Financial support.* This research has been supported by the National Natural Science Foundation of China
570 (42227901), Southern Marine Science and Engineering Guangdong Laboratory (Zhuhai), grant number
571 SML2020SP007 and SML2021SP207; the Innovation Group Project of Southern Marine Science and
572 Engineering Guangdong Laboratory (Zhuhai), grant number 311020004 and 311022001; the National
573 Natural Science Foundation of China, grant number 42206005; the open fund of State Key Laboratory of
574 Satellite Ocean Environment Dynamics, Second Institute of Oceanography, MNR, grant number QNHX2309;
575 General scientific research project of Zhejiang Provincial Department of Education, grant number
576 Y202250609; the Open Foundation from Marine Sciences in the First-Class Subjects of Zhejiang, grant number
577 OFMS006; State Key Laboratory of Tropical Oceanography (South China Sea Institute of Oceanology Chinese
578 Academy of Sciences), grant number LTO2220.

579

580

581

582 **References**

583 Cabanes, C., Grouazel, A., von Schuckmann, K., Hamon, M., Turpin, V., Coatanoan, C., Guinehut, S.,
584 Boone, C., Ferry, N., and Reverdin, G.: The CORA dataset: validation and diagnostics of ocean
585 temperature and salinity in situ measurements, *Ocean Sci. Discuss.*, 9, 1273-1312, 2012.
586 Chen, G., Hou, Y., and Chu, X.: Mesoscale eddies in the South China Sea: Mean properties,
587 spatiotemporal variability, and impact on thermohaline structure, *J. Geophys. Res.: Oceans*,
588 116, <https://doi.org/10.1029/2010jc006716>, 2011.

589 Chen Z, Yu F, Chen Z, et al. Downward Propagation and Trapping of Near-Inertial Waves by a
590 Westward-moving Anticyclonic Eddy in the Subtropical Northwestern Pacific Ocean[J]. *Journal of*
591 *Physical Oceanography*, 2023.

592 de Boyer Montégut, C.: Mixed layer depth over the global ocean: An examination of profile data and a
593 profile-based climatology, *J. Geophys. Res.: Oceans*, 109,<https://doi.org/10.1029/2004jc002378>, 2004.

594 Ezraty, R., Girard-Ardhuin, F., Piollé, J.-F., Kaleschke, L., and Heygster, G.: Arctic and Antarctic sea
595 ice concentration and Arctic sea ice drift estimated from Special Sensor Microwave data, Département
596 d’Océanographie Physique et Spatiale, IFREMER, Brest, France and University of Bremen Germany, 2,
597 2007.

598 Huang, L., Cao, R., and Zhang, S.: Distribution and Oceanic Dynamic Mechism of Precipitation Induced
599 by Typhoon Lekima, *American Journal of Climate Change*, 11, 133-
600 154,<https://doi.org/10.4236/ajcc.2022.112007>, 2022.

601 Huang, X. and Wang, G.: Response of a Mesoscale Dipole Eddy to the Passage of a Tropical Cyclone:
602 A Case Study Using Satellite Observations and Numerical Modeling, *Remote Sens.*,
603 14,<https://doi.org/10.3390/rs14122865>, 2022.

604 Jaimes, B. and Shay, L. K.: Enhanced Wind-Driven Downwelling Flow in Warm Oceanic Eddy Features
605 during the Intensification of Tropical Cyclone Isaac (2012): Observations and Theory, *J. Phys. Oceanogr.*,
606 45, 1667-1689,<https://doi.org/10.1175/jpo-d-14-0176.1>, 2015.

607 Jullien, S., Menkès, C. E., Marchesiello, P., Jourdain, N. C., Lengaigne, M., Koch-Larrouy, A., Lefèvre,
608 J., Vincent, E. M., and Faure, V.: Impact of tropical cyclones on the heat budget of the South Pacific
609 Ocean, *J. Phys. Oceanogr.*, 42, 1882-1906,<https://doi.org/10.1175/JPO-D-11-0133.1>, 2012.

610 Kessler, W. S.: The circulation of the eastern tropical Pacific: A review, *Prog. Oceanogr.*, 69, 181-
611 217,<https://doi.org/10.1016/j.pocean.2006.03.009>, 2006.

612 Li, Q., Sun, L., Liu, S., Xian, T., and Yan, Y.: A new mononuclear eddy identification method with
613 simple splitting strategies, *Remote Sens. Lett.*, 5, 65 - 72,<https://doi.org/10.1080/2150704x.2013.872814>,
614 2014.

615 Li, X., Zhang, X., Fu, D., and Liao, S.: Strengthening effect of super typhoon Rammasun (2014) on
616 upwelling and cold eddies in the South China Sea, *J. Oceanol. Limnol.*, 39, 403-
617 419,<https://doi.org/10.1007/s00343-020-9239-x>, 2021.

618 Lin, I. I., Chou, M.-D., and Wu, C.-C.: The Impact of a Warm Ocean Eddy on Typhoon Morakot (2009):
619 A Preliminary Study from Satellite Observations and Numerical Modelling, *TAO: Terrestrial,*
620 *Atmospheric and Oceanic Sciences*, 22,[https://doi.org/10.3319/tao.2011.08.19.01\(tm\)](https://doi.org/10.3319/tao.2011.08.19.01(tm)), 2011.

621 Lin, I. I., Wu, C.-C., Emanuel, K. A., Lee, I. H., Wu, C.-R., and Pun, I.-F.: The Interaction of
622 Supertyphoon Maemi (2003) with a Warm Ocean Eddy, *Mon. Weather Rev.*, 133, 2635-
623 2649,<https://doi.org/10.1175/MWR3005.1>, 2005.

624 Liu, F. and Tang, S.: Influence of the Interaction Between Typhoons and Oceanic Mesoscale Eddies on
625 Phytoplankton Blooms, *J. Geophys. Res.: Oceans*, 123, 2785-
626 2794,<https://doi.org/10.1029/2017jc013225>, 2018.

627 Liu, S.-S., Sun, L., Wu, Q., and Yang, Y.-J.: The responses of cyclonic and anticyclonic eddies to
628 typhoon forcing: The vertical temperature-salinity structure changes associated with the horizontal
629 convergence/divergence, *J. Geophys. Res.: Oceans*, 122, 4974-
630 4989,<https://doi.org/10.1002/2017JC012814>, 2017.

631 Lu, Z., Wang, G., and Shang, X.: Response of a Preexisting Cyclonic Ocean Eddy to a Typhoon, *J. Phys.*
632 *Oceanogr.*, 46, 2403-2410,<https://doi.org/10.1175/jpo-d-16-0040.1>, 2016.

633 Lu, Z., Wang, G., and Shang, X.: Strength and Spatial Structure of the Perturbation Induced by a Tropical
634 Cyclone to the Underlying Eddies, *J. Geophys. Res.: Oceans*, 125,<https://doi.org/10.1029/2020jc016097>,
635 2020.

636 Lu, Z., Wang, G., and Shang, X.: Observable large-scale impacts of tropical cyclones on subtropical gyre,
637 *J. Phys. Oceanogr.*,<https://doi.org/10.1175/JPO-D-22-0230.1>, 2023.

638 Ma, Z., Zhang, Z., Fei, J., and Wang, H.: Imprints of Tropical Cyclones on Structural Characteristics of
639 Mesoscale Oceanic Eddies Over the Western North Pacific, *Geophys. Res. Lett.*,
640 48,<https://doi.org/10.1029/2021gl092601>, 2021.

641 Ma, Z., Fei, J., Liu, L., Huang, X., and Li, Y.: An Investigation of the Influences of Mesoscale Ocean
642 Eddies on Tropical Cyclone Intensities, *Mon. Weather Rev.*, 145, 1181-
643 1201,<https://doi.org/10.1175/mwr-d-16-0253.1>, 2017.

644 Ning, J., Xu, Q., Zhang, H., Wang, T., and Fan, K.: Impact of Cyclonic Ocean Eddies on Upper Ocean
645 Thermodynamic Response to Typhoon Soudelor, *Remote Sens.*, 11,<https://doi.org/10.3390/rs11080938>,
646 2019.

647 Oey, L. Y., Ezer, T., Wang, D. P., Fan, S. J., and Yin, X. Q.: Loop Current warming by Hurricane Wilma,
648 *Geophys. Res. Lett.*, 33,<https://doi.org/10.1029/2006gl025873>, 2006.

649 Price, J. F.: Upper Ocean Response to a Hurricane, *J. Phys. Oceanogr.*,[https://doi.org/10.1175/1520-0485\(1981\)011%3C0153:UORTAH%3E2.0.CO;2](https://doi.org/10.1175/1520-0485(1981)011%3C0153:UORTAH%3E2.0.CO;2), 1981.

651 Pujol, M.-I., Faugère, Y., Taburet, G., Dupuy, S., Pelloquin, C., Ablain, M., and Picot, N.: DUACS
652 DT2014: the new multi-mission altimeter data set reprocessed over 20 years, *Ocean Sci.*, 12, 1067-
653 1090,<https://doi.org/10.5194/os-12-1067-2016>, 2016.

654 Rudzin, J. E. and Chen, S.: On the dynamics of the eradication of a warm core mesoscale eddy after the
655 passage of Hurricane Irma (2017), *Dyn. Atmos. Oceans*,
656 100,<https://doi.org/10.1016/j.dynatmoce.2022.101334>, 2022.

657 Shang, X.-d., Zhu, H.-b., Chen, G.-y., Xu, C., and Yang, Q.: Research on Cold Core Eddy Change and
658 Phytoplankton Bloom Induced by Typhoons: Case Studies in the South China Sea, *Adv. Meteorol.*, 2015,
659 1-19,<https://doi.org/10.1155/2015/340432>, 2015.

660 Shay, L. K. and Jaimes, B.: Mixed Layer Cooling in Mesoscale Oceanic Eddies during Hurricanes
661 Katrina and Rita, *Mon. Weather Rev.*, 137, 4188-4207,<https://doi.org/10.1175/2009mwr2849.1>, 2009.

662 Shay, L. K. and Jaimes, B.: Near-Inertial Wave Wake of Hurricanes Katrina and Rita over Mesoscale
663 Oceanic Eddies, *J. Phys. Oceanogr.*, 40, 1320-1337,<https://doi.org/10.1175/2010jpo4309.1>, 2010.

664 Shay, L. K., Goni, G. J., and Black, P. G.: Effects of a Warm Oceanic Feature on Hurricane Opal, *Mon.*
665 *Weather Rev.*, 128, 1366-1383,[https://doi.org/10.1175/1520-0493\(2000\)128<1366:EOAWOF>2.0.CO;2](https://doi.org/10.1175/1520-0493(2000)128<1366:EOAWOF>2.0.CO;2), 2000.

667 Song, D., Guo, L., Duan, Z., and Xiang, L.: Impact of Major Typhoons in 2016 on Sea Surface Features
668 in the Northwestern Pacific, *Water*, 10,<https://doi.org/10.3390/w10101326>, 2018.

669 Sun, J., Ju, X., Zheng, Q., Wang, G., Li, L., and Xiong, X.: Numerical Study of the Response of Typhoon
670 Hato (2017) to Grouped Mesoscale Eddies in the Northern South China Sea, *J. Geophys. Res.: Atmos.*,
671 128,<https://doi.org/10.1029/2022jd037266>, 2023.

672 Sun, L., Yang, Y., Xian, T., Lu, Z., and Fu, Y.: Strong enhancement of chlorophyll a concentration by a
673 weak typhoon, *Mar. Ecol. Prog. Ser.*, 404, 39-50,<https://doi.org/10.3354/meps08477>, 2010.

674 Sun, L., Li, Y.-X., Yang, Y.-J., Wu, Q., Chen, X.-T., Li, Q.-Y., Li, Y.-B., and Xian, T.: Effects of super
675 typhoons on cyclonic ocean eddies in the western North Pacific: A satellite data-based evaluation

676 between 2000 and 2008, *J. Geophys. Res.: Oceans*, 119, 5585-
677 5598,<https://doi.org/10.1002/2013jc009575>, 2014.

678 Thompson, B. and Tkalich, P.: Mixed layer thermodynamics of the Southern South China Sea, *Clim.*
679 *Dyn.*, 43, 2061-2075,<https://doi.org/10.1007/s00382-013-2030-3>, 2014.

680 Wada, A. and Usui, N.: Impacts of Oceanic Preexisting Conditions on Predictions of Typhoon Hai-Tang
681 in 2005, *Adv. Meteorol.*, 2010, 756071,<https://doi.org/10.1155/2010/756071>, 2010.

682 Walker, N. D., Leben, R. R., and Balasubramanian, S.: Hurricane-forced upwelling and
683 chlorophyllaenhancement within cold-core cyclones in the Gulf of Mexico, *Geophys. Res. Lett.*, 32, n/a-
684 n/a,<https://doi.org/10.1029/2005gl023716>, 2005.

685 Wang, G., Su, J., Ding, Y., and Chen, D.: Tropical cyclone genesis over the south China sea, *J. Mar.*
686 *Syst.*, 68, 318-326,<https://doi.org/10.1016/j.jmarsys.2006.12.002>, 2007.

687 Wang, G., Zhao, B., Qiao, F., and Zhao, C.: Rapid intensification of Super Typhoon Haiyan: the
688 important role of a warm-core ocean eddy, *Ocean Dyn.*, 68, 1649-1661,[https://doi.org/10.1007/s10236-](https://doi.org/10.1007/s10236-018-1217-x)
689 [018-1217-x](https://doi.org/10.1007/s10236-018-1217-x), 2018.

690 Xiu, P., Chai, F., Shi, L., Xue, H., and Chao, Y.: A census of eddy activities in the South China Sea
691 during 1993–2007, *J. Geophys. Res.: Oceans*, 115,<https://doi.org/10.1029/2009jc005657>, 2010.

692 Yan, Y., Li, L., and Wang, C.: The effects of oceanic barrier layer on the upper ocean response to tropical
693 cyclones, *J. Geophys. Res.: Oceans*, 122, 4829-4844,<https://doi.org/10.1002/2017jc012694>, 2017.

694 Yu, F., Yang, Q., Chen, G., and Li, Q.: The response of cyclonic eddies to typhoons based on satellite
695 remote sensing data for 2001–2014 from the South China Sea, *Oceanologia*, 61, 265-
696 275,<https://doi.org/10.1016/j.oceano.2018.11.005>, 2019.

697 Yu, J., Lin, S., Jiang, Y., and Wang, Y.: Modulation of Typhoon-Induced Sea Surface Cooling by
698 Preexisting Eddies in the South China Sea, *Water*, 13,<https://doi.org/10.3390/w13050653>, 2021.

699 Zhang, H.: Modulation of Upper Ocean Vertical Temperature Structure and Heat Content by a Fast-
700 Moving Tropical Cyclone, *J. Phys. Oceanogr.*, 53, 493-508,<https://doi.org/10.1175/jpo-d-22-0132.1>,
701 2022.

702 Zhang, H., Chen, D., Zhou, L., Liu, X., Ding, T., and Zhou, B.: Upper ocean response to typhoon
703 Kalmaegi (2014), *J. Geophys. Res.: Oceans*, 121, 6520-6535,<https://doi.org/10.1002/2016jc012064>,
704 2016.

705 Zhang, Y., Zhang, Z., Chen, D., Qiu, B., and Wang, W.: Strengthening of the Kuroshio current by
706 intensifying tropical cyclones, *Science*, 368, 988-993,<https://doi.org/10.1126/science.aax5758>, 2020.

707